

Improvement of the microstructure and magnetic properties of (La,Ce)-Fe-B nanocrystalline ribbons

Li-Yu Lian(连李昱), Xiao-Wei Zhang(张晓伟), Ying Liu(刘颖), Jun Li(李军), and Ren-Quan Wang(王仁全)
Citation: Chin. Phys. B, 2023, 32 (**7**): 077501. DOI: 10.1088/1674-1056/acd8ae
Journal homepage: http://cpb.iphy.ac.cn; http://iopscience.iop.org/cpb

What follows is a list of articles you may be interested in

Coercivity enhancement of sintered Nd-Fe-B magnets by grain boundary diffusion with $Pr_{80-x}Al_xCu_{20}$ alloys

Zhe-Huan Jin(金哲欢), Lei Jin(金磊), Guang-Fei Ding(丁广飞), Shuai Guo(郭帅), Bo Zheng(郑波),Si-Ning Fan(樊思宁), Zhi-Xiang Wang(王志翔), Xiao-Dong Fan(范晓东), Jin-Hao Zhu(朱金豪),Ren-Jie Chen(陈仁杰), A-Ru Yan(闫阿儒), Jing Pan(潘晶), and Xin-Cai Liu(刘新才)
Chin. Phys. B, 2023, 32 (**1**): 017505. DOI: 10.1088/1674-1056/ac6741

Magnetic properties and resistivity of a 2:17-type SmCo magnet doped with ZrO_2

Qi-Qi Yang(杨棋棋), Zhuang Liu(刘壮), Chao-Yue Zhang(张超越), Hai-Chen Wu(吴海辰), Xiao-Lei Gao(高晓磊), Yi-Long Ma(马毅龙), Ren-Jie Chen(陈仁杰), and A-Ru Yan(闫阿儒)
Chin. Phys. B, 2021, 30 (**7**): 077504. DOI: 10.1088/1674-1056/abf7a9

Effects of post-sinter annealing on microstructure and magnetic properties of Nd-Fe-B sintered magnets with Nd-Ga intergranular addition

Jin-Hao Zhu(朱金豪), Lei Jin(金磊), Zhe-Huan Jin(金哲欢), Guang-Fei Ding(丁广飞), Bo Zheng(郑波), Shuai Guo(郭帅), Ren-Jie Chen(陈仁杰), and A-Ru Yan(闫阿儒)
Chin. Phys. B, 2021, 30 (**6**): 067503. DOI: 10.1088/1674-1056/abddad

Texture analysis of ultra-high coercivity Sm_2Co_7 hot deformation magnets

Qiang Ma(马强), Meishuang Jia(贾美爽), Zhifeng Hu(胡智峰), Ming Yue(岳明), Yanli Liu(刘艳丽), Tongyun Zhao(赵同云), and Baogen Shen(沈保根)
Chin. Phys. B, 2021, 30 (**4**): 047505. DOI: 10.1088/1674-1056/abe2fc

Coercivity and microstructure of sintered Nd-Fe-B magnets diffused with Pr-Co, Pr-Al, and Pr-Co-Al alloys

Lei Jin(金磊), Zhe-Huan Jin(金哲欢), Jin-Hao Zhu(朱金豪), Guang-Fei Ding(丁广飞), Bo Zheng(郑波) , Shuai Guo(郭帅), Ren-Jie Chen(陈仁杰), A-Ru Yan(闫阿儒), and Xin-Cai Liu(刘新才)
Chin. Phys. B, 2021, 30 (**2**): 027503. DOI: 10.1088/1674-1056/abc166

Improvement of the microstructure and magnetic properties of (La,Ce)–Fe–B nanocrystalline ribbons

Li-Yu Lian(连李昱)[1], Xiao-Wei Zhang(张晓伟)[1], Ying Liu(刘颖)[1,2], Jun Li(李军)[1,†], and Ren-Quan Wang(王仁全)[1]

[1] *School of Materials Science and Engineering, Sichuan University, Chengdu* 610065, *China*

[2] *Key Laboratory of Advanced Special Material & Technology, Ministry of Education, Sichuan University, Chengdu* 610065, *China*

(Received 28 March 2023; revised manuscript received 10 May 2023; accepted manuscript online 25 May 2023)

The obstacles of inferior microstructure and poor magnetic properties of (La,Ce)–Fe–B type magnets stand in the way of expanding their applications. In this work, (La,Ce)–Fe–B melt-spun ribbons were prepared with different La/Ce ratios and rare earth contents. The microstructure and magnetic properties of these ribbons were investigated. With the La/Ce ratio increased, the fraction of the $CeFe_2$ phase decreased and the β-La phase segregated among matrix grains, which deteriorated the coercivity of the ribbons. Reducing the rare earth content effectively suppressed the β-La phase and improved the proportion of the matrix phase in the ribbons. Here, the optimal alloy composite $(La_{15}Ce_{85})_{14}Fe_{80}B_6$ has been obtained with modified microstructure and inhibited secondary phases. Good ribbon performance was tested, with $H_{cj} = 4.51$ kOe, $B_r = 6.29$ kG and $(BH)_{max} = 6.81$ MGOe.

Keywords: (La,Ce)–Fe–B, La/Ce ratio, rare earth content, secondary phases inhibition

PACS: 75.50.Ww, 75.47.Lx, 75.75.–c **DOI:** 10.1088/1674-1056/acd8ae

1. Introduction

To curb the cost of permanent magnet production, the cost-effective Ce–Fe–B[1–3] and (La,Ce)–Fe–B[4–9] rare earth permanent magnets have attracted wide attention. Herbst *et al.*[10,11] and Soeda *et al.*[12] reported the hard magnetic properties of $Ce_2Fe_{14}B$ and $(La,Ce)_2Fe_{14}B$ compounds, respectively. With the addition of Hf,[13] Ta[14] and Ga[15,16] to Ce–Fe–B type magnets, finer matrix phase grains and good magnetic properties have been obtained. However, the secondary phases (such as $CeFe_2$, β-La phases, etc.) in these magnets result in deterioration of the microstructure and poor magnetic properties.[15,17] Recent investigations have been made on elemental dopants to inhibit secondary phases. Zhang *et al.*[18] and Rehman *et al.*[19] reported that Si and Ge atoms enter into the lattice of the $CeFe_2$ phase and suppress the generation of the $CeFe_2$ phase. The growth of the matrix phase grains and the formation of the $CeFe_2$ phase have been inhibited by the addition of Mo.[20] In comparison, fewer reports have focused on the effect on secondary phase inhibition of light rare earth elements substituted for Ce.

Our previous study investigated the contribution of La to expanding the formation temperature gap between $(La,Ce)_2Fe_{14}B$ and metastable Ce_2Fe_{17} phases.[21] Recent work on $(La,Ce)_2Fe_{14}B$ alloys[22] verified the relationship between phase consistency and magnetic properties. Unlike elemental dopant methods, La atoms may enter into the $Ce_2Fe_{14}B$ phase lattice and improve the magnetic properties.[23] Therefore, our understanding of the effect of La on variation of the microstructure and magnetic properties in (La,Ce)–Fe–B ribbons still needs to be clarified.

In this work, (La,Ce)–Fe–B ribbons with different La/Ce ratios and rare earth element contents were prepared. The relationship between the microstructure of ribbons and the magnetic performance was investigated. A fine microstructure was obtained in ribbons with good magnetic properties.

2. Experimental method

Two kinds of cast ingots were prepared by induction melting: Ce–Fe–B type alloy and (La,Ce)–Fe–B type alloy. The Ce–Fe–B type alloy had the nominal compositions of $Ce_zFe_{94-z}B_6$ (z = 12, 13, 14, 15, 16) and the (La,Ce)–Fe–B type alloy had nominal compositions of $(La_yCe_{100-y})_xFe_{94-x}B_6$ (x = 12, 14, 16 and y = 0, 15, 25, 35, 50). The constituent metals had a purity better than 99.8 wt.% and the whole process of casting took place under an argon atmosphere. The cast ingot was remelted in a quartz tube for the homogenization of alloy composition, followed by rapid quenching at a molybdenum wheel at a speed of 45 m·s^{-1}. The rapidly quenched ribbons were placed in a tube furnace and heated at 525 °C for 15 min under a vacuum to ensure their complete crystallization. Standard bonded magnets were prepared to verify the magnetic properties of the ribbons. The mixture, combining the magnetic powder with epoxy resin in the proportion of 100:2.5, was pressed into a cylinder with a density of about 6.0 g·cm^{-3}. These bonded magnets were solidified at 175 °C for 90 min.

†Corresponding author. E-mail: li_jun@scu.edu.cn

© 2023 Chinese Physical Society and IOP Publishing Ltd

The phase constitution and structure of Ce–Fe–B type and (La,Ce)–Fe–B type alloys were characterized by an x-ray diffraction (XRD) analyzer with Cu K_α radiation ($\lambda = 1.54$ Å) and Co K_α radiation ($\lambda = 1.79$ Å), respectively, over a 2θ range of 20°–70°. The refinement results were calculated by the Rietveld method via general structure analysis system (GSAS) software.[24] Magnetic properties were measured with a vibrating sample magnetometer (VSM; Lakeshore 7410) by applying a maximum magnetic field of 2.5 T. The hysteresis curves were corrected with a demagnetization factor (N) equal to 0.21.[25] Bonded magnets were measured by an automatic measuring instrument for magnetization characteristic (AMT-4). The morphology of the ribbons was investigated by a scanning electron microscope (FEI Inspect F50) and a transmission electron microscope (TEM; FEI Talos F200X) equipped with energy dispersive x-ray spectroscopy (EDX; Super X). The equivalent diameter data were collected via Image Pro Plus (IPP) software with counts of at least 300.

3. Results and discussion

3.1. Phase constitution and magnetic properties of Ce–Fe–B type alloys

To understand the phase variation in Ce–Fe–B alloys, melt ribbons with Ce content changed from 12 at.% to 16 at.%. were prepared. Figure 1(a) shows the XRD pattern of each crystallized ribbon. It is noteworthy that the secondary phase ($CeFe_2$) emerges when the Ce content is 14 at.%. Due to the Curie temperature of the $CeFe_2$ phase being much lower than room temperature (about 225 K),[26] this secondary phase exhibits paramagnetism under the working condition of permanent magnets. Meanwhile, the relative intensity of the diffraction peaks of the $CeFe_2$ phase in the alloy was enhanced with the growing concentration of Ce, which means that the weight fraction of $CeFe_2$ in ribbons grew simultaneously.

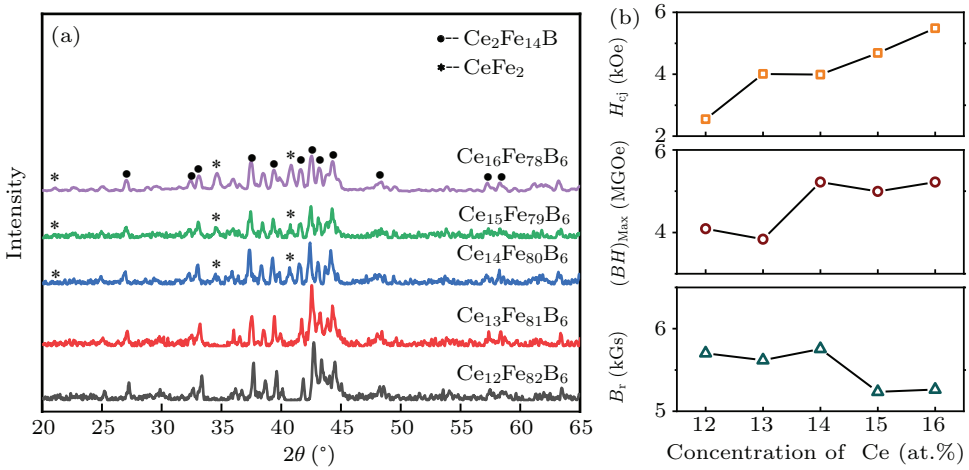


Fig. 1. XRD patterns of Ce–Fe–B alloys (a) and the magnetic properties of Ce–Fe–B ribbons (b).

The magnetic properties of Ce–Fe–B type alloys with rare earth element contents from 12 at.% to 16 at.% were tested with a VSM and are shown in Fig. 1(b). The variation of coercivity for the ribbons shared the same trend as the Ce content in the alloys, but a slight lump was found in the magnetic remanence plot. The $Ce_{16}Fe_{78}B_6$ ribbon exhibited the best comprehensive properties, with $H_{cj} = 5.4$ kOe and $(BH)_{max} = 5.22$ MGOe, respectively. Grigoras *et al.*[27] and Li *et al.*[28] investigated such a phenomenon for the evolution of magnetic properties with variation in the rare earth content, which may be attributed to the phase constitution in alloys. Recent investigations[29,30] reported that the paramagnetic $CeFe_2$ phase would effectively isolate and decouple the matrix phase grains. In addition, due to the good wettability of the Ce-rich phase, it would flow into the gap between matrix grains and form grain boundaries (GBs).[31] The exchange coupling effect would be weakened if GBs individually isolated matrix phase grains. Moreover, the relatively low solidification point of the intergranular phase may smooth the edge of hard magnetic phase grains. The regularization of matrix grains in ribbons would lead to a decrease in the effective demagnetization factor (N_{eff}) and improve coercivity. As a result of these factors, the coercivity of Ce–Fe–B type alloy is increased as the Ce content increases. Meanwhile, the proportion of the $Ce_2Fe_{14}B$ (2:14:1) phase in Ce–Fe–B type alloys should also be addressed, as this would directly affect the magnetic properties of ribbons. Thus, the increasing concentration of Ce would generate more $CeFe_2$ phase and dilute the magnetic remanence of the ribbons.

3.2. Effects of La/Ce ratio on the microstructure and magnetic properties

A rare earth element content of 16 at.% was selected for its excellent performance in Ce–Fe–B type ribbons. The Rietveld refinement patterns for different y values in $(La_yCe_{100-y})_{16}Fe_{78}B_6$ ribbons are exhibited in Fig. 2(a). The

lattice parameters of the $RE_2Fe_{14}B$ phase (RE = rare earth) and the phase composition of each ribbon are listed in Table 1. With y increasing from 0% to 25%, the mass fraction of the $CeFe_2$ phase drops from 21.027 wt.% to 1.911 wt.%. When y reaches 35%, the 1:2 phase is completely suppressed by La. Due to the instability of the (La,Ce)Fe_2 phase[32] and the expanded gap in the formation temperature between (La,Ce)$_2Fe_{14}B$ and metastable Ce_2Fe_{17} phases,[21,33] the $CeFe_2$ phase is gradually suppressed with the increasing La/Ce ratio. Given the relatively high temperature (796.75 °C) of the invariant reaction (L↔ α-Fe+β-La),[34] the β-La phase formed when the La ratio varied from 15% to 50% and the mass fraction of the β-La phase increased drastically from 0.294 wt.% to 4.025 wt.%. The γ-Ce phase[35] is a product of a eutectic reaction at about 604 °C following the formula L↔$CeFe_2$ + γ-Ce and was found in $(La_yCe_{100-y})_{16}Fe_{78}B_6$ ribbons with a high Ce content. Because La atoms may dissolve into the γ-Ce phase, the γ-Ce phase was named the RE-rich phase in this work. With an increasing La/Ce ratio and β-La phase generation, the fraction of the RE-rich phase decreased from 7.468 wt.% to 0.009 wt.% in $(La_yCe_{100-y})_{16}Fe_{78}B_6$ alloys.

As the substitution of La increased from 0% to 50%, the lattice parameters of $(La_yCe_{100-y})_{16}Fe_{78}B_6$ ribbons expanded with a near-linear trend, as shown in Table 1 and Fig. 2(b). Because of the larger atomic radius of La compared with Ce, the substitution of La atoms for Ce atoms in the 2:14:1 phase would bring about an expansion of lattice space. Therefore, an increasing La/Ce ratio promotes more La atoms to occupy Ce lattice sites in the $Ce_2Fe_{14}B$ tetragonal lattice.

To clarify the elemental distribution in ribbons, TEM and EDX mapping studies for different La/Ce ratios were performed, as shown in Fig. 3. The bright-field TEM images for $Ce_{16}Fe_{78}B_6$, $(La_{15}Ce_{85})_{16}Fe_{78}B_6$ and $(La_{35}Ce_{65})_{16}Fe_{78}B_6$ are demonstrated in Figs. 3(a), 3(b) and 3(c), respectively. Fe, Ce, B and La were selected for mapping scanning and the detected regions are exhibited in Figs. 3(d)–3(l). The concentration of rare earth elements in $(La_yCe_{100-y})_{16}Fe_{78}B_6$ alloys is excessive for formation of the matrix phase. Hence, the aggregation of rare earth elements is inevitable, as reflected in Figs. 3(e), 3(h), 3(i), 3(k) and 3(l). With the La/Ce ratio increased, the aggregating areas of La expanded. The positive formation energy[36] of $La_2Fe_{14}B$ may induce more serious segregation of La than Ce. Notably, a large area of La segregation (with a length of about 112.16 nm) is found in Fig. 3(l). This critical aggregation may accelerate the consumption of excessive rare earth atoms in the $(La_{35}Ce_{65})_{16}Fe_{78}B_6$ ribbon.

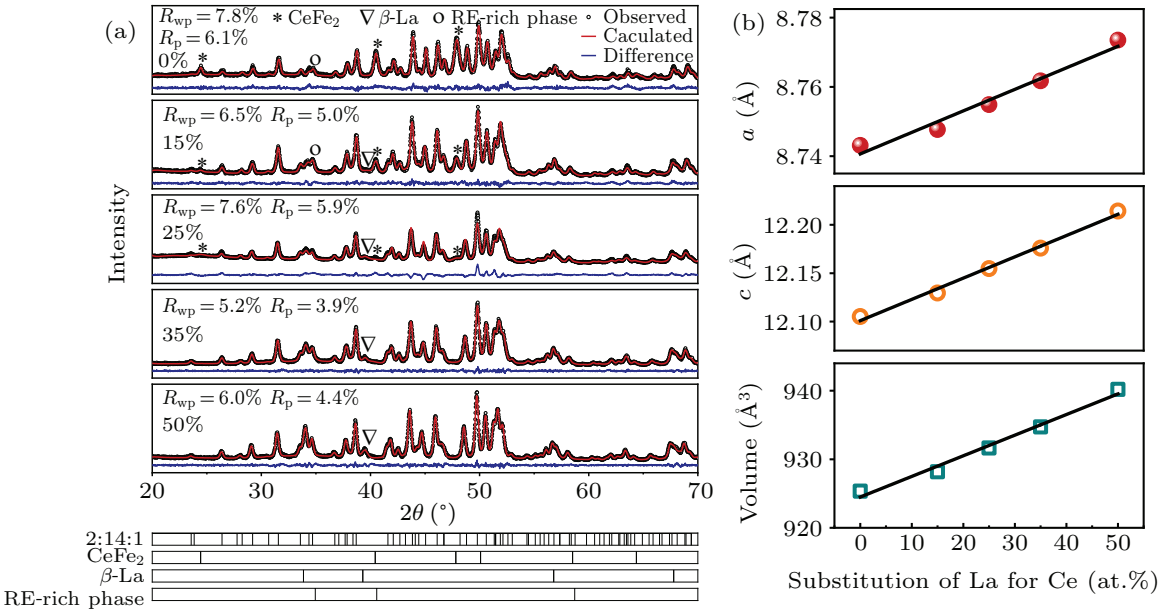


Fig. 2. XRD patterns of $(La_yCe_{100-y})_{16}Fe_{78}B_6$ alloys (a) and the refined lattice parameters for $(La_{-}Ce_{100-y})_{16}Fe_{78}B_6$ alloys (b).

Table 1. The refined lattice parameters and phase fractions of $(La_yCe_{100-y})_{16}Fe_{78}B_6$ alloys.

	Lattice parameters of $RE_2Fe_{14}B$			Phase fraction (wt.%)			
	a (Å)	c (Å)	V (Å^3)	$RE_2Fe_{14}B$	$CeFe_2$	β-La	RE-rich
$Ce_{16}Fe_{78}B_6$	8.743	12.105	925.346	71.505	21.027	/	7.468
$(La_{15}Ce_{85})_{16}Fe_{78}B_6$	8.747	12.132	928.279	83.886	8.741	0.294	7.079
$(La_{25}Ce_{75})_{16}Fe_{78}B_6$	8.755	12.155	931.639	93.519	1.911	3.757	0.813
$(La_{35}Ce_{65})_{16}Fe_{78}B_6$	8.762	12.176	934.715	96.085	/	3.212	0.703
$(La_{50}Ce_{50})_{16}Fe_{78}B_6$	8.774	12.210	940.185	95.966	/	4.025	0.009

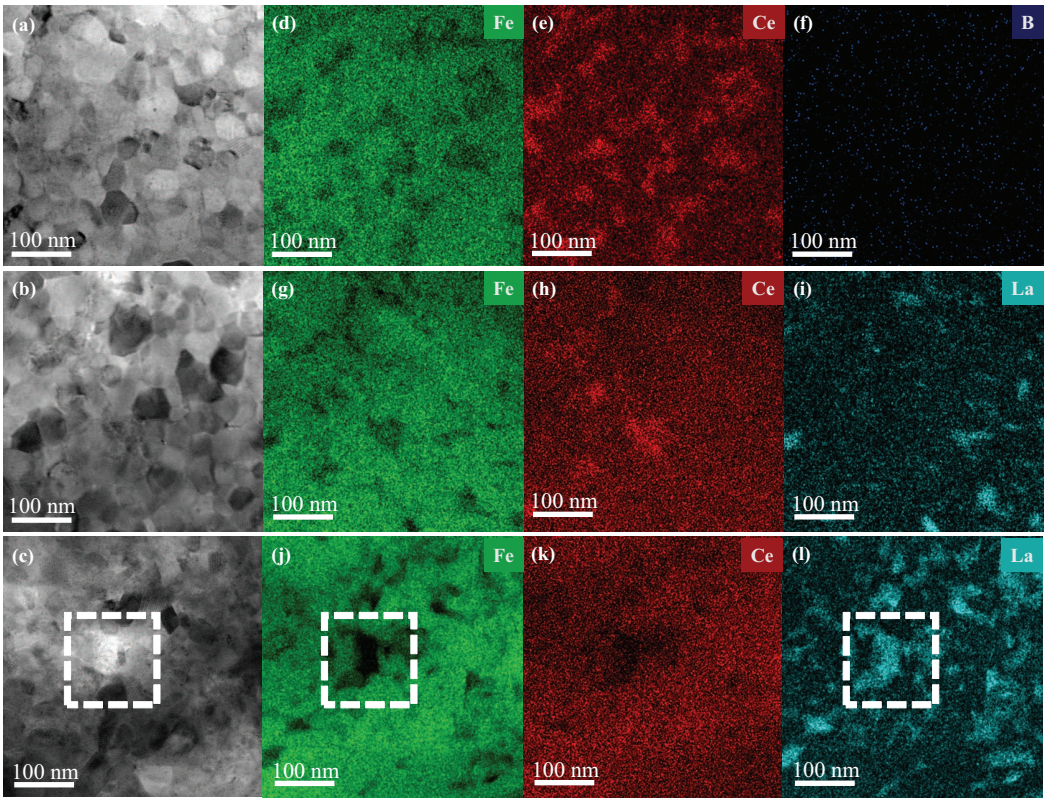


Fig. 3. Bright-field (BF) TEM images for the rapidly quenching ribbons: $Ce_{16}Fe_{78}B_6$ (a), $(La_{15}Ce_{85})_{16}Fe_{78}B_6$ (b) and $(La_{35}Ce_{65})_{16}Fe_{78}B_6$ (c). The TEM-EDX elemental mappings of each ribbon are shown in (d)–(l).

The TEM images of ribbons for $Ce_{16}Fe_{78}B_6$, $(La_{15}Ce_{85})_{16}Fe_{78}B_6$ and $(La_{35}Ce_{65})_{16}Fe_{78}B_6$ are exhibited in Figs. 4(a_1), 4(a_2) and 4(a_3). Figure 4(b_1) shows the high-resolution TEM (HRTEM) image of the orange square area in Fig. 4(a_1). It shows the region far from the secondary phase in the $Ce_{16}Fe_{78}B_6$ ribbon. A 2:14:1 phase grain was confirmed via a fast Fourier transformation (FFT) pattern, as shown in Fig. 4(c_1). By virtue of the high fraction of rare earth-rich phase in the $Ce_{16}Fe_{78}B_6$ alloy, rare earth atoms were gathered in this region, and GBs (with a thickness of about 7.62 nm) were formed between 2:14:1 phase grains. The EDX line scanning results for the GBs are exhibited in Fig. 4(d_1). This further proved that the composition of GBs is enriched with rare earth elements. Figure 4(b_2) shows a similar area remote to the secondary phase in the $(La_{15}Ce_{85})_{16}Fe_{78}B_6$ ribbon and is marked with an orange square in Fig. 4(a_2). The adjacent matrix grains were confirmed via FFT patterns in Figs. 4(c_2) and 4(e_2). Clear GBs (with a thickness of about 3.53 nm) were formed between them and are exhibited in an enlarged image in Fig. 4(d_2). The orange square in Fig. 4(a_3) is the area far from the secondary phase in the $(La_{35}Ce_{65})_{16}Fe_{78}B_6$ ribbon. In the HRTEM image (Fig. 4(b_3)) of this area, matrix grains were confirmed by FFT patterns in Figs. 4(c_3)–4(e_3). However, there is no obvious GB around these matrix phase grains.

The $CeFe_2$ phase exists in regions marked with red squares in Figs. 4(a_1) and 4(a_2), these being TEM images for the $Ce_{16}Fe_{78}B_6$ ribbon and the $(La_{15}Ce_{85})_{16}Fe_{78}B_6$ ribbon, respectively. HRTEM images of these areas are shown in Figs. 4(e_1) and 4(f_2), respectively. The $CeFe_2$ phase grains were verified from the FFT images in Figs. 4(f_1) and 4(g_2). These 1:2 phase grains are distributed in the triple junctions among matrix grains that directly contact each other, as shown in Figs. S1(a_1–f_1) and (a_2–d_2).

The β-La phase grains were found in $(La_{15}Ce_{85})_{16}Fe_{78}B_6$ and are marked with a blue square in Fig. 4(a_2). Figure 4(h_2) shows the HRTEM image of this blue square, and the β-La phase grains were confirmed by the FFT pattern in Fig. 4(i_2). The large segregation area of La in $(La_{35}Ce_{65})_{16}Fe_{78}B_6$ ribbons is marked with a blue square in Fig. 4(a_3). The HRTEM and FFT images of the segregation area are shown in Figs. 4(f_3) and 4(i_3). It is noticeable that a β-La phase grain formed in this segregation region. Figures 4(g_3) and 4(h_3) are FFT images for neighboring 2:14:1 phase grains. However, there is no apparent intergranular phase between adjacent matrix phase grains that are next to the β-La phase, as shown in Figs. S1(e_2)–(k_2).

Statistical graphs of the equivalent diameter (D) of matrix phase grains for $Ce_{16}Fe_{78}B_6$, $(La_{15}Ce_{85})_{16}Fe_{78}B_6$ and $(La_{35}Ce_{65})_{16}Fe_{78}B_6$ ribbons are exhibited in Figs. 5(a)–5(c), respectively. When the La/Ce ratio changed from 0% to 35%, the mean equivalent diameter of the matrix grains increased from 33.7 nm to 37.4 nm.

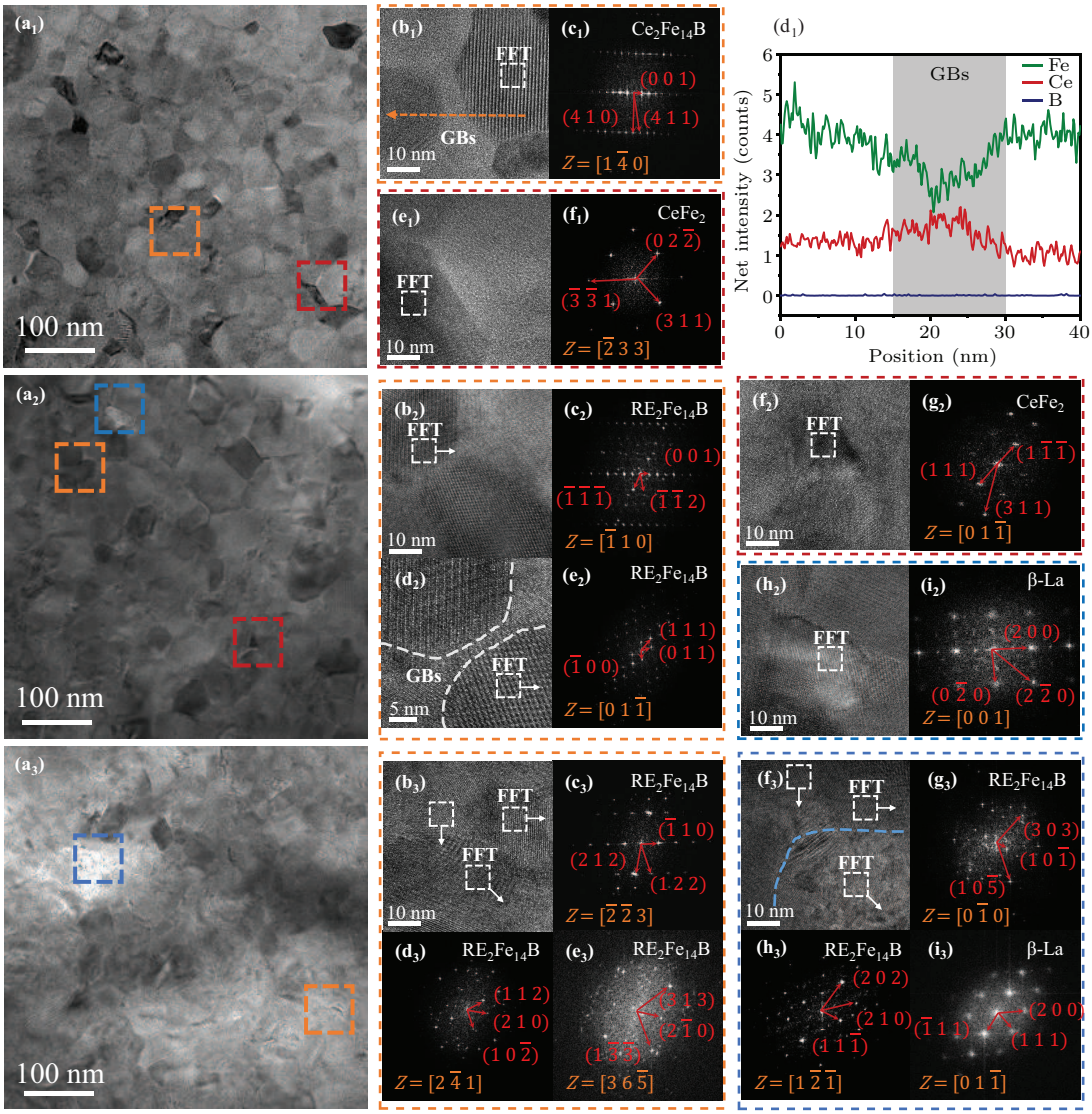


Fig. 4. Bright-field TEM images for the rapidly quenching ribbons $Ce_{16}Fe_{78}B_6$ (a_1), $(La_{15}Ce_{85})_{16}Fe_{78}B_6$ (a_2) and $(La_{35}Ce_{65})_{16}Fe_{78}B_6$ (a_3). Areas remote to secondary phases are marked as orange squares in (a_1), (a_2) and (a_3). The high-resolution TEM (HRTEM) and fast Fourier transformation (FFT) images for the orange squares are shown in (b_1) and (c_1), (b_2) and (e_2) and (b_3) and (e_3), respectively. The EDX line scanning result for the grain boundaries of (b_1) is shown in (d_1). The $CeFe_2$ phase exists in areas marked as red squares in (a_1) and (a_2). The HRTEM and FFT images for the red squares are shown in (e_1) and (f_1) and (f_2) and (g_2), respectively. The β-La phase exists in areas marked as blue squares in (a_2) and (a_3). The HRTEM and FFT images for blue squares are shown in (h_2) and (i_2) and (f_3) and (i_3), respectively.

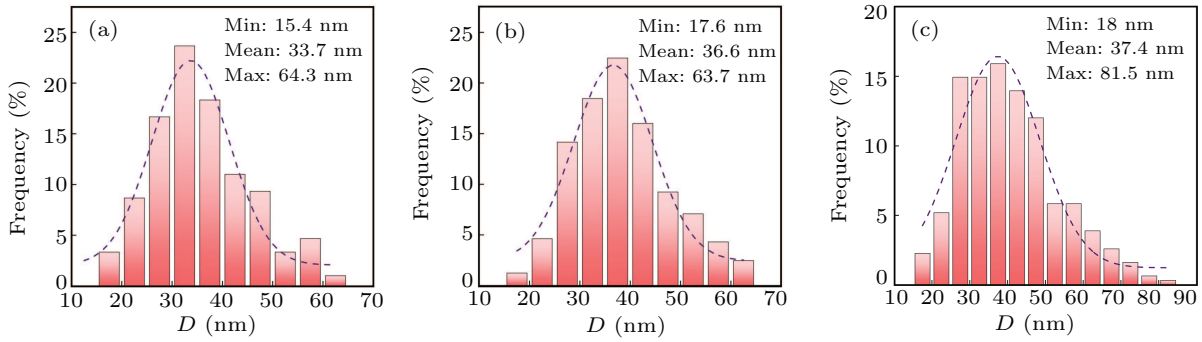


Fig. 5. Statistical graphs of the equivalent diameter of matrix phase grains in $Ce_{16}Fe_{78}B_6$ (a), $(La_{15}Ce_{85})_{16}Fe_{78}B_6$ (b) and $(La_{35}Ce_{65})_{16}Fe_{78}B_6$ (c) ribbons.

Figure S2 shows the results of EDX mapping studies of areas containing rare earth-rich and β-La phases, respectively. For the area where a rare earth-rich phase is present (Fig. S2(a)), the elements are homogeneously distributed, as shown in Figs. S2(b)–(d). Benefiting from the good mobility of the rare earth-rich phase, the length of the segregation area of Ce is as little as 12.6 nm. Therefore, in $Ce_{16}Fe_{78}B_6$ and $(La_{15}Ce_{85})_{16}Fe_{78}B_6$ ribbons, the relatively high fraction

of the rare earth-rich phase would promote sufficient rare earth atoms to form GBs. For $(La_{35}Ce_{65})_{16}Fe_{78}B_6$ ribbons, in comparison, the rare earth-rich phase fraction (0.703 wt.%) is too low to enclose matrix grains. Moreover, the formation of the β-La phase consumed excessive rare earth atoms and was aggregated in the junctions among matrix phase grains, as shown in Figs. S2(e)–(h). Both factors are responsible for the deterioration of ribbon microstructure, especially on the GBs.

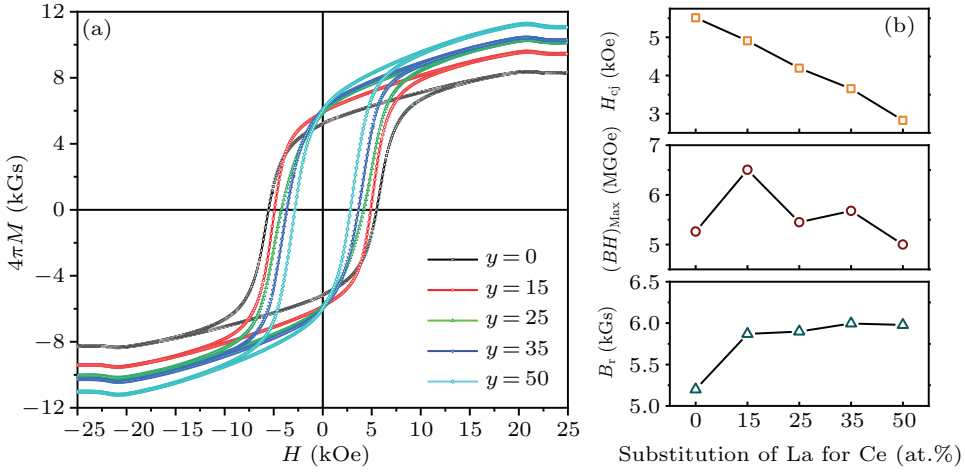


Fig. 6. The hysteresis loops of $(La_yCe_{100-y})_{16}Fe_{78}B_6$ alloys (a) and the magnetic parameters for $(La_yCe_{100-y})_{16}Fe_{78}B_6$ alloys (b).

The magnetic properties of ribbons are closely related to their phase composition and microstructure. Figures 6(a) and 6(b) show the hysteresis loops and magnetic properties of $(La_yCe_{100-y})_{16}Fe_{78}B_6$ ($y = 0$, 15, 25, 35, 50) ribbons. The maximum magnetic energy product of 6.5 MGOe was obtained in $(La_{15}Ce_{85})_{16}Fe_{78}B_6$ ribbon. During the increase in La ratio, the B_r of the ribbons grew from 5.2 kG to 6.0 kG, but the H_{cj} value dropped from 5.5 kOe to 3.3 kOe.

Due to the suppression of $CeFe_2$ by La in (La,Ce)–Fe–B ribbons, the relative content of the matrix phase and the magnetic remanence are improved. Furthermore, referring to the density functional theory results calculated by Alam *et al.*[37] the valence of the Ce element is sensitive to the environment of atoms in the crystal lattice. The expansion of the $Ce_2Fe_{14}B$ lattice space would promote the valence to a +3 state, which means the magnetic moment of a single crystal would be enhanced.[38] As a result, the ribbon's magnetic remanence was improved after La substituted for Ce in the alloy.

The size of matrix phase grains increased with increase in the La/Ce ratio, leading to the deterioration of coercivity. Meanwhile, based on the results of theoretical calculations, the anisotropy field (H_A) of the $La_2Fe_{14}B$ compound (20 kOe)[10] is lower than that of the $Ce_2Fe_{14}B$ compound (26 kOe). When La atoms entered the $Ce_2Fe_{14}B$ lattice structure, the $(La,Ce)_2Fe_{14}B$ matrix phase would be formed with a relatively lower H_A than $Ce_2Fe_{14}B$.[21] In addition, as the La content increased, fractions of the rare earth-rich phase and the $CeFe_2$ phase decreased, strengthening the exchange coupling effect between matrix phase grains.[17] The large segregation area of the β-La phase would generate poor GBs between matrix grains,[4] and they may act as nucleation sites for the reverse magnetization domains and worsen the H_{cj} of ribbons. In summary, all these factors would induce the deterioration of coercivity in $(La,Ce)_{16}Fe_{78}B_6$.

3.3. Effects of rare earth content on microstructure and magnetic properties

Due to the inhibitory effect on the $CeFe_2$ phase and the relatively low fraction of the β-La phase, a proportion of 15% of La in (La,Ce)–Fe–B alloy was selected as the optimal La/Ce ratio. The Rietveld refinement results for $(La_{15}Ce_{85})_{12}Fe_{82}B_6$ and $(La_{15}Ce_{85})_{14}Fe_{80}B_6$ ribbons are given in Fig. 7 and Table 2. The paramagnetic $CeFe_2$ and the β-La phases are faded in $(La_{15}Ce_{85})_{14}Fe_{80}B_6$ and $(La_{15}Ce_{85})_{12}Fe_{82}B_6$ alloys. The $CeFe_2$ phase was wholly suppressed in $(La_{15}Ce_{85})_{14}Fe_{80}B_6$ alloy shown by the low relative intensity of $CeFe_2$ in the

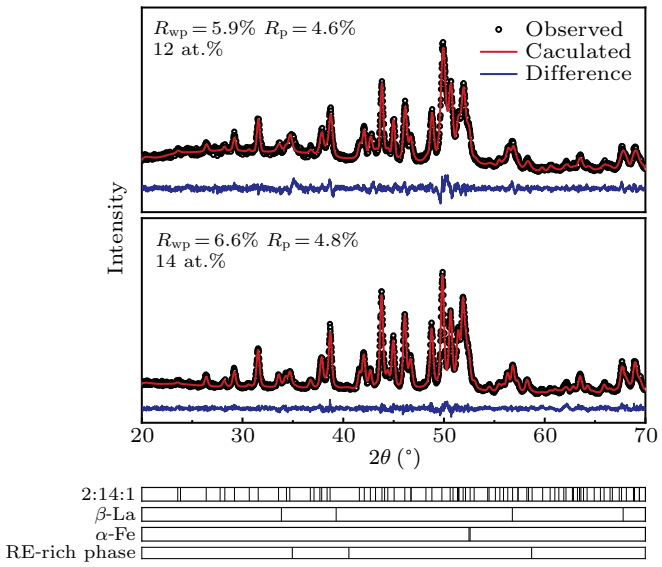


Fig. 7. XRD pattern of $(La_{15}Ce_{85})_{12}Fe_{82}B_6$ and $(La_{15}Ce_{85})_{14}Fe_{80}B_6$ alloys.

XRD pattern of $Ce_{14}Fe_{80}B_6$. With the reducing content of La, the formation of the β-La phase was suppressed in the $(La_{15}Ce_{85})_{14}Fe_{80}B_6$ ribbon with a low fraction of 0.123 wt.%. With the smaller rare earth content in the $(La_{15}Ce_{85})_{14}Fe_{80}B_6$ ribbon than in the $(La_{15}Ce_{85})_{16}Fe_{78}B_6$ ribbon, the fraction of the rare earth-rich phase declined from 7.079 wt.% to 0.962 wt.%. However, because of the repulsion between La and Fe[39,40] in forming a compound, the α-Fe phase forms in $(La_{15}Ce_{85})_{12}Fe_{82}B_6$ ribbon with a phase fraction of 1.87 wt.%.

For $(La_{15}Ce_{85})_{14}Fe_{80}B_6$ alloy, the La content is higher than in $(La_{15}Ce_{85})_{12}Fe_{82}B_6$ alloy. This may promote more La atoms to enter into the matrix phase lattice and generate a greater lattice space. In comparison, the lattice parameters are much closer for $x = 14$ at.% and 16 at.% alloys, in agreement with a previous report.[23]

The TEM results for $(La_{15}Ce_{85})_{12}Fe_{82}B_6$ and $(La_{15}Ce_{85})_{14}Fe_{80}B_6$ ribbon are shown in Fig. 8. Figure 8(b_4) is the enlarged bright-field TEM image for the area marked with a green square in Fig. 8(a_4). An EDX mapping study for Fe, Ce and La in this area was done and the results are shown in Figs. 8(c_4)–8(e_4). In $(La_{15}Ce_{85})_{12}Fe_{82}B_6$ ribbon, a large Fe segregation region (with a length of about 65.13 nm) was found, and the α-Fe phase was confirmed via the FFT pattern (Fig. 8(f_4)) in this region. The 2:14:1 phase next to this region was verified by the FFT image in Fig. 8(g_4).

Table 2. The refined lattice parameters and phase fractions of $(La_{15}Ce_{85})_{16}Fe_{78}B_6$, $(La_{15}Ce_{85})_{14}Fe_{80}B_6$ and $(La_{15}Ce_{85})_{12}Fe_{82}B_6$ alloys.

	Lattice parameters of $RE_2Fe_{14}B$			Phase fraction (wt.%)				
	a (Å)	c (Å)	V (Å^3)	$RE_2Fe_{14}B$	$CeFe_2$	α-Fe	β-La	RE-rich
$(La_{15}Ce_{85})_{16}Fe_{78}B_6$	8.747	12.132	928.279	83.886	8.741	/	0.294	7.079
$(La_{15}Ce_{85})_{14}Fe_{80}B_6$	8.753	12.138	929.968	98.915	/	/	0.123	0.962
$(La_{15}Ce_{85})_{12}Fe_{82}B_6$	8.740	12.131	926.724	98.130	/	1.870	/	/

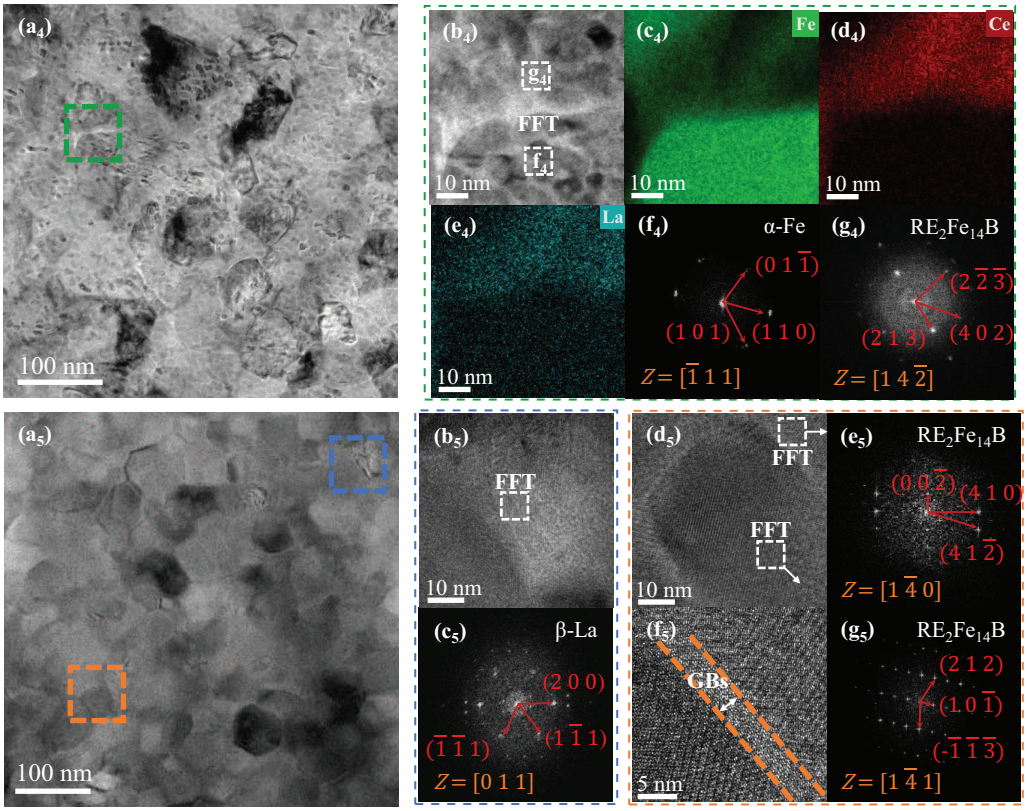


Fig. 8. Bright-field TEM images for the rapidly quenching ribbons $(La_{15}Ce_{85})_{12}Fe_{82}B_6$ (a_4) and $(La_{15}Ce_{85})_{14}Fe_{80}B_6$ (a_5). The α-Fe phase exists in the area marked as the green square in (a_4). The bright-field TEM images and the TEM-EDX elemental mappings of the green square are shown in (b_4) and (e_4). Parts (f_4) and (g_4) show FFT images for areas marked with white squares in (b_4). The β-La phase exists in the area marked with a blue square in (a_5). The HRTEM and FFT images for the blue square are shown in (b_5) and (c_5). The area remote to the β-La phase is marked as an orange squares in (a_5). The HRTEM and FFT images for the orange square are shown in (d_5) and (g_5).

Figure 8(b_5) is the HRTEM image of the region marked with a blue square in Fig. 8(a_5). The β-La phase in this region was confirmed by the FFT pattern (Fig. 8(c_5)). In this region, the GBs between neighboring matrix grains are obscure. The area far from the β-La grains is marked with an orange square in Fig. 8(a_5). Clear GBs have been formed with a thickness of 2.75 nm, as displayed in Fig. 8(d_5) and enlarged in Fig. 8(f_5). Both grains were confirmed as the matrix phase via FFT im-

ages in Figs. 8(e_5) and 8(g_5). The reduction of the rare earth content inhibits the formation of secondary phases (the $CeFe_2$ and β-La phases) and curbs the consumption of excessive rare earth elements. Thus, the rare earth-rich phase remained in $(La_{15}Ce_{85})_{14}Fe_{82}B_6$ ribbon with a fraction of 0.962 wt.%, and clear GBs can be generated between the matrix phase grains.

The variation of magnetic properties and the hysteresis loops of $(La_{15}Ce_{85})_xFe_{94-x}B_6$ ($x = 12$, 14, 16) ribbons are shown in Fig. 9(a). As the rare earth element content decreases, the coercivity of the melt-spun ribbons dropped from 4.9 kOe to 2.5 kOe. On the contrary, the B_r of stripes attained a peak of 6.29 kG when $x = 14$ at.%. The magnetic remanence of the $(La_{15}Ce_{85})_{12}Fe_{82}B_6$ ribbon is lower than that of the $(La_{15}Ce_{85})_{14}Fe_{80}B_6$ ribbon by 0.2 kG. Compared with the $(La_{15}Ce_{85})_{16}Fe_{78}B_6$ ribbon, the H_{cj} value of the $(La_{15}Ce_{85})_{14}Fe_{80}B_6$ ribbon decreased slightly by 0.4 kOe. This may be due to the contribution of the inhibition of secondary phases and the formation of GBs in the $(La_{15}Ce_{85})_{14}Fe_{80}B_6$ ribbon. The optimal $(BH)_{max}$ (6.81 MGOe) was achieved in $(La_{15}Ce_{85})_{14}Fe_{80}B_6$ ribbons with $H_{cj} = 4.51$ kOe. A best $(BH)_{max}$ of 4.5 MGOe for $(La_{15}Ce_{85})_{14}Fe_{80}B_6$ bonded magnet was obtained, as shown in Fig. 9(b).

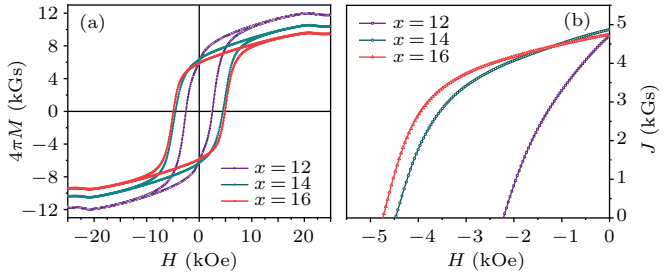


Fig. 9. The hysteresis loops of $(La_{15}Ce_{85})_xFe_{94-x}B_6$ ribbons (a) and the demagnetization curves of bonded $(La_{15}Ce_{85})_xFe_{94-x}B_6$ magnets (b).

In the $(La_{15}Ce_{85})_{12}Fe_{82}B_6$ ribbon, the exchange coupling effect exists between hard–soft magnetic grains and hard magnetic grains.[41] The large size of the α-Fe phase grain prevented complete exchange hardening of the soft magnetic phase.[42] Furthermore, the large soft magnetic area in the ribbon weakened the exchange coupling effect between matrix grains.[43] Thus, the $(La_{15}Ce_{85})_{12}Fe_{82}B_6$ ribbon had lower coercivity and magnetic remanence than the $(La_{15}Ce_{85})_{14}Fe_{80}B_6$ ribbon. Thinner GBs and a lower fraction of secondary phases were obtained in the $y = 14$ ribbon, which could explain the slightly lower coercivity and stronger remanence than for the $y = 16$ one, which had a more robust exchange interaction. To sum up, a declining rare earth content decreases the weight of secondary phases and heightens the intergranular exchange coupling between the matrix phase grains.

4. Conclusion

In this work, the phase composition and microstructure of (La,Ce)–Fe–B rapidly quenching ribbons have been modified via a reasonable composition design. The solute behavior of La atoms entering into the matrix phase lattice has been discussed. An increasing ratio of La in (La,Ce)–Fe–B induces a near-liner expansion of lattice parameters and variation of the intrinsic properties in the matrix phase. Due to the decline of H_A and the enhancement of magnetic moment that occurred in the 2:14:1 phase lattice, the magnetic properties of ribbons would be affected. In the alloy with a relatively high rare earth content (16 at.%), the formation of secondary phases (the $CeFe_2$ and β-La phases) is hard to avoid and would result in microstructural deterioration. Reducing the rare earth content suppressed the formation of these secondary phases and strengthened the exchange coupling effect between grains. A fine microstructure with a shallow secondary phase fraction was obtained in the $(La_{15}Ce_{85})_{14}Fe_{80}B_6$ ribbon. Good magnetic properties with $(BH)_{max} = 6.81$ MGOe, $H_{cj} = 4.51$ kOe and $B_r = 6.29$ kG were found for the $(La_{15}Ce_{85})_{14}Fe_{80}B_6$ ribbon. A bonded magnet with $(BH)_{max} = 4.5$ MGOe was prepared.

Acknowledgement

Project supported by the fifth batch of major scientific and technological research projects in the Panxi Experimental Zone of Sichuan Province, the new functional materials and applications of rare earth vanadium titanium (Grant No. 2020SCUNG201).

References

[1] Sun Q, Zhu M, Wang Q, Zhu C, Yang J and Li W 2023 *Acta. Mater.* **246** 118703
[2] Pathak A K, Khan M, Gschneidner K A, Jr., McCallum R W, Zhou L, Sun K, Dennis K W, Zhou C, Pinkerton F E, Kramer M J and Pecharsky V K 2015 *Adv. Mater.* **27** 2663
[3] Wang R, Liu Y, Li J, Zhao W and Yang X 2017 *Mater. Res. Express.* **4** 046104
[4] Chen H, Li Y, Zhang H, Liu W, Wu H, Qin Y, Yue M, Wei Q, Zhang B and Di J 2023 *Adv. Sci.* **10** 2301312
[5] Liu Y L, Ma Q, Wang X, Zhou J J, Zhao T Y, Hu F X, Sun J R and Shen B G 2020 *Chin. Phys. B* **29** 107504
[6] Lin X, Luo Y, Peng H, Yang Y, Dou Y, Wang Z, Xu K, Diao S and Yu D 2019 *J. Magn. Magn. Mater.* **490** 165454
[7] Hussain M, Zhao L Z, Akram R, Ahmad Z, Zhang Z Y, Gulzar A, Zhong X C and Liu Z W 2018 *J. Magn. Magn. Mater.* **468** 141
[8] Tang D, Liu Y, Li J, Liu X and Zhou Q 2018 *J. Magn. Magn. Mater.* **460** 263
[9] Yan M, Jin J and Ma T 2019 *Chin. Phys. B* **28** 077507
[10] Herbst J F 1991 *Rev. Mod. Phys.* **63** 819
[11] Herbst J F, Meyer M S, and Pinkerton F E 2012 *J. Appl. Phys.* **111** 07a718
[12] H. Soeda M Y, Yamasaki J and Mohri K 1985 *IEEE Transl. J. Magn. Jpn.* **1** 1006
[13] Jiang Q, Zhong M, Quan Q, Lei W, Zeng Q, Hu Y, Xu Y, Hu X, Zhang L, Liu R, Ma S and Zhong Z 2017 *J. Magn. Magn. Mater.* **444** 344
[14] Zhang J S, Li W, Liao X F, Yu H Y, Zhao L Z, Zeng H X, Peng D R and Liu Z W 2019 *J. Mater. Sci. Technol.* **35** 1877
[15] Wang R Q, Shen X, Liu Y and Li J 2016 *IEEE Trans. Magn.* **52** 2101806
[16] Jiang Q, Zhong M, Lei W, Zeng Q, Hu Y, Quan Q, Xu Y, Hu X, Zhang L, Liu R, Ma S and Zhong Z 2017 *AIP. Adv.* **7** 085013
[17] Wang R Q, Liu Y, Li J, Zhao W and Yang X J 2017 *J. Mater. Sci.* **52** 7311

[18] Zhang J S, Zhao L Z, Liao X F, Zeng H X, Peng D R, Yu H Y, Zhong X C and Liu Z W 2019 *Intermetallics* **107** 75

[19] Rehman S U, Jiang Q, Liu K, He L, Ouyang H, Zhang L, Wang L, Ma S and Zhong Z 2019 *J. Phys. Chem. Solids.* **132** 182

[20] Grigoras M, Lostun M, Borza F, Porcescu M and Lupu N 2022 *Intermetallics* **141** 107425

[21] Shi Q, Liu Y, Li J, Zhao W, Wang R and Gao X 2019 *J. Magn. Magn. Mater.* **476** 1

[22] Liao X F, Zhao L Z, Zhang J S, Ahmed G, Khan A J, Zeng H X, Yu H Y, Zhong X C, Liu Z W and Zhang G Q 2019 *Curr. Appl. Phys.* **19** 733

[23] Liao X F, Zhang J S, Yu H Y, Zhong X C, Zhao L Z, Xu K, Peng D R and Liu Z W 2019 *J. Mater. Sci.* **54** 7288

[24] Toby B H 2001 *J. Appl. Crystallogr.* **34** 210

[25] Zhongmin C, Smith B R and Bao.Min M 2002 *IEEE Trans. Magn.* **38** 2976

[26] Rehman S U, Ouyang H, Jiang Q, Liu K, He L, Song J, Wang L, Luo X, Ma S and Zhong Z 2019 *J. Magn. Magn. Mater.* **486** 165252

[27] Grigoras M, Lostun M, Stoian G, Herea D D, Chiriac H and Lupu N 2017 *J. Magn. Magn. Mater.* **432** 119

[28] Li Z, Zhang M, Shen B, Hu F and Sun J 2016 *Mater. Lett.* **172** 102

[29] Feng H B, Chen X S and Li A H 2021 *J. Magn. Magn. Mater.* **522** 167493

[30] Wu J X, Zhao X T, Liu W, Li Y, Ma J, Song Y H, Liu L, Ju H Z and Zhang Z D 2022 *J. Appl. Phys.* **131** 163901

[31] Feng H, Zhang Y, Li A, Zhao Y and Li W 2017 *IEEE Trans. Magn.* **53** 3302004

[32] Li Z, Yue M, Liu X, Zhang H, Liu W, Li Y and Zhang Z 2020 *J. Magn. Magn. Mater.* **505** 166747

[33] Yan C J, Guo S, Chen R J, Lee D and Yan A R 2014 *Chin. Phys. B* **23** 107501

[34] Su D, Yang K C, Rong M H, Liu P P, Yao Q R, Wang J, Chen Q, Rao G H and Zhou H Y 2023 *Calphad* **80** 102506

[35] Xi L, Li A, Feng H, Tan M, Sun W, Zhu M and Li W 2019 *J. Rare Earths.* **37** 865

[36] Liu X B, Altounian Z, Huang M, Zhang Q and Liu J P 2013 *J. Alloys Compd.* **549** 366

[37] Alam A, Khan M, McCallum R W and Johnson D D 2013 *Appl. Phys. Lett.* **102** 042402

[38] Xu K, Li H, Luo Y, Wang L, Yu D, Wang Z, Peng H and Zhang Y 2018 *J. Magn. Magn. Mater.* **461** 100

[39] Wei Q, Lu Z, Yao Q, Deng J, Wang J, Zhou H and Rao G 2021 *Trans. Nonferrous Met. Soc. China.* **31** 1748

[40] Liu X B and Nlebedim I C 2023 *AIP. Adv.* **13** 025211

[41] Kneller E F and Hawig R 1991 *IEEE Trans. Magn.* **27** 3588

[42] R. Fischer T S, Kronmüller H and Fidler J 1996 *J. Magn. Magn. Mater.* **153** 35

[43] Li Z B, Zhang M, Shen B G and Sun J R 2013 *Appl. Phys. Lett.* **102** 102405